

# Compact localized states and magnetic flux-driven topological phase transition in a diamond-dodecagon lattice geometry

Joydeep Majhi<sup>1,\*</sup> and Biplab Pal<sup>2,†</sup>

<sup>1</sup>*AbCMS Lab, Department of Metallurgical Engineering and Materials Science, Indian Institute of Technology Bombay, Mumbai, Maharashtra, 400076, India*

<sup>2</sup>*Department of Physics, School of Sciences, Nagaland University, Lumami 798627, Nagaland, India*

(Dated: February 16, 2026)

We propose and investigate a novel two-dimensional (2D) tight-binding model defined on a diamond-dodecagon lattice geometry that hosts multiple flat bands (FBs) and supports topological phase transitions driven by a magnetic flux. This lattice exhibits three completely flat, non-dispersive bands in the band structure in the absence of magnetic flux due to destructive interference in the electron hoppings, leading to the emergence of compact localized states (CLS). These CLS are analytically constructed and exhibit real-space confinement of the electrons, arising solely due to the lattice's geometrical frustration. It has been shown that these FBs are very robust against the introduction of weak random onsite disorder in the system. By tuning the uniform magnetic flux threaded through the diamond plaquettes, we demonstrate a tunable evolution of the band structure and show that certain bands develop nontrivial topological features with nonzero integer values of the Chern number. Additionally, we have computed the multi-terminal transport properties for this 2D lattice system, which display the flux-tunable resonances and transmission suppression linked to the FBs, establishing a clear interplay between the localization, topology, and transport. Our findings put forward the diamond-dodecagon lattice as a robust and tunable platform for studying the flat-band physics and magnetic flux-controlled topological phenomena, offering promising experimental feasibility in photonic lattices and ultracold atomic systems.

## I. INTRODUCTION

The exploration of flat-band (FB) systems has gained considerable attention in recent years due to their rich physical properties and potential applications in the emergent quantum materials [1–3]. Characterized by dispersionless energy eigenstates with zero group velocity and effectively infinite mass, flat bands (FBs) arise from the intricate interplay of the lattice geometry and destructive interference in hopping pathways. This leads to a macroscopic degeneracy of single-particle states, effectively quenching the kinetic energy and allowing interaction effects to dominate. FB systems not only host a wide array of exotic many-body phases, such as high-temperature superconductivity [4–8], flat-band ferromagnetism [9–12], and fractional Chern insulators [13–15], but also draw fundamental significance from their deep analogy to Landau levels in two-dimensional electron gases, which underpin the celebrated integer and fractional quantum Hall effects [16–18]. From both theoretical and experimental perspectives, FB systems play a pivotal role in understanding the synergy between geometry, topology, and electron correlations in engineered lattice systems.

The microscopic origin of FBs in tight-binding lattice models is rooted in destructive quantum interference, which suppresses the particle hopping between certain lattice sites and leads to the formation of compact local-

ized states (CLS) [19–22]. These eigenstates are characterized by wavefunctions confined to a finite set of lattice sites, with amplitudes vanishing identically outside this region. The existence and structure of CLS are closely tied to the lattice's topology and symmetry, making them a defining feature of geometrical frustration [23]. Such FB localization mechanisms have been demonstrated across a range of geometries, including the Lieb [24, 25], Kagome [25, 26], dice [25, 27], and diamond chain lattices [28–30], as well as in various artificially engineered lattices [31–38]. Many of these systems support one or more FBs due to their unique connectivity patterns, and recent experimental advances have enabled the physical realization of such FBs in photonic crystals [39–42], ultracold atom systems [43–45], and moiré heterostructures [46–48], providing highly tunable platforms for studying FB physics in controlled environments. Very recently, FB lattice settings have also been proposed for the realization of robust quantum storage devices [49].

A compelling frontier in the flat-band research is the engineering of band topology through external perturbations. Of particular interest is the introduction of magnetic flux through lattice plaquettes [21, 22, 26, 29, 30, 32, 43], which modifies the hopping phases via the Peierls substitution and allows the generation of nontrivial topological features. These include topological flat bands (TFBs) that possess finite Berry curvature and are associated with quantized Chern numbers, akin to Landau levels in a continuum, but without the requirement of a magnetic field [50–52]. While perfect flatness, finite-range hopping, and nontrivial topology cannot coexist in a single band due to theoretical constraints [53], TFBs remain promising candidates for hosting fractional Chern insula-

\* E-mail: [joydeepmjh@gmail.com](mailto:joydeepmjh@gmail.com)

† Corresponding author; E-mail: [biplab@nagalanduniversity.ac.in](mailto:biplab@nagalanduniversity.ac.in)

tors – lattice analogs of fractional quantum Hall states, potentially stable at higher temperatures.

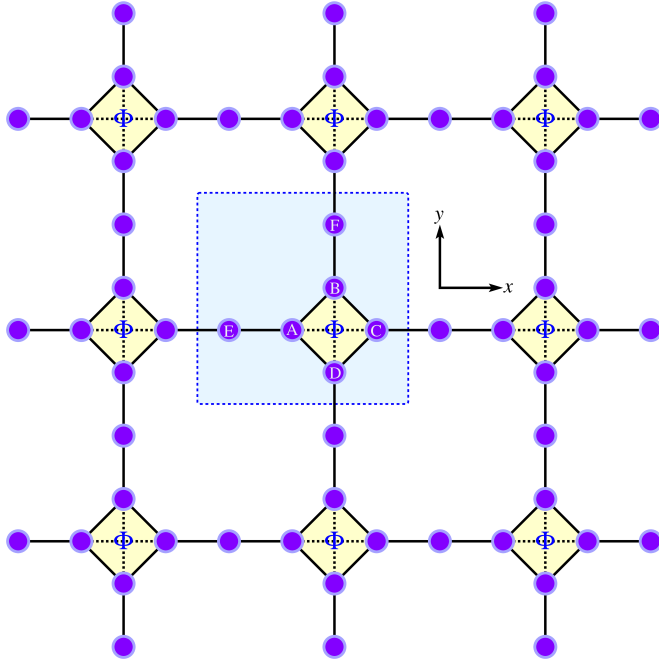


FIG. 1. Schematic diagram of a two-dimensional (2D) diamond-dodecagon lattice model. The unit cell of the lattice containing six atomic sites is highlighted with light blue color. Each diamond plaquette is pierced by a uniform magnetic flux  $\Phi$ . The solid black lines represent the nearest-neighbor hopping and the dotted lines represent the next-nearest-neighbor hopping.

In this work, we propose and investigate a novel two-dimensional lattice model, termed as “diamond-dodecagon lattice”, which exhibits a rich flat-band structure and nontrivial topological phases. The key findings in this study lies in the systematic control of both flat band formation and topological properties through the interplay between an externally tunable magnetic flux and the intrinsic lattice hopping parameters. The unit cell of this lattice consists of six atomic sites arranged in a 2D geometry composed of interconnected diamond and dodecagon plaquettes. A uniform magnetic flux  $\Phi$  is introduced through each diamond plaquette (see Fig. 1), which breaks the time-reversal symmetry, leading to complex hopping amplitudes governed by the Aharonov-Bohm phase [54]. The tight-binding Hamiltonian includes both nearest-neighbor hopping along the edges of the plaquettes and diagonal hopping inside the diamond plaquettes (see Fig. 1), thereby incorporating the geometrical frustration and interference effects in a systematic way.

Our analysis reveals the presence of three completely flat bands for this lattice model in the absence of the magnetic flux, associated with CLS that exhibit nontrivial spatial amplitude distributions. These CLS can be analytically constructed and are characterized by van-

ishing wavefunction amplitudes on specific sub-lattices, a hallmark of the destructive interference. We demonstrate that the application of magnetic flux leads to a gradual dispersion of the FBs, highlighting the tunability of the spectrum via an external control. We further explore the topological character of the bands by computing their Berry curvatures and Chern numbers as a function of the magnetic flux. For selected flux values ( $\Phi = \Phi_0/4$  and  $\Phi_0/2$ ), we find the emergence of nonzero integer values of the Chern numbers in specific bands, confirming the topological nature of these bands.

To probe the transport properties of the finite system, we construct a scattering geometry by attaching semi-infinite leads along the  $\pm x$  directions of a  $10 \times 10$  diamond-dodecagon lattice. By calculating the two-terminal transmission probability as a function of the injection energy and magnetic flux, we observe distinct signatures of FB transport, including sharp resonant features and flux-dependent transmission suppression. These results demonstrate the potential of this model to act as a flux-tunable quantum transport device. Our findings establish the diamond-dodecagon lattice as a promising candidate for realizing and studying FB physics along with controllable topological and transport properties. The model’s simplicity, combined with its capacity for magnetic tunability and the presence of robust compact localized states, makes it an attractive framework for the experimental implementation in photonic as well as in ultracold atomic systems. Moreover, the interplay between flatness, topology, and transport uncovered for this lattice model offers a deeper insight into the design principles necessary for engineering topological FB materials.

The remainder of this paper is organized as follows: Sec. II introduces the tight-binding Hamiltonian of the diamond-dodecagon lattice and presents a detailed analysis of the band structure as a function of the magnetic flux and the hopping parameters. Sec. III demonstrates the explicit construction of the CLS corresponding to the FBs and analyzes their spatial structure along with the computation of the density of states. Sec. IV examines the topological properties of the model through systematic calculations of the Berry curvatures and Chern numbers, establishing the topological phase diagram. Sec. V investigates the transport properties of the finite system with attached leads, revealing the signatures of the FB physics in the transmission spectra. Finally, in Sec. VI, we conclude with a summary of our key findings and an outlook on the future directions, including the role of interactions and potential applications in quantum devices.

## II. THE LATTICE MODEL AND THE SPECTRUM

### A. Geometry and Real-Space Hamiltonian

We investigate a 2D tight-binding model defined on a periodic lattice composed of interconnected diamond and

dodecagon plaquettes, hence referred to as the *diamond-dodecagon* lattice. The unit cell consists of six atomic sites, labelled as  $A, B, C, D, E$ , and  $F$ , as illustrated in Fig. 1. Each diamond plaquette is threaded by a uniform magnetic flux  $\Phi$ , which induces a Peierls phases in the hopping amplitudes along the arms of the diamond plaquettes. This magnetic flux serves as a crucial tuning parameter that allows systematic control over both the band structure and topological properties of the system. The dodecagon plaquettes provide additional connectivity that enhances the geometric frustration, while main-

taining the overall lattice periodicity. The lattice extends periodically along the both  $x$ - and  $y$ -directions.

The system includes two types of hopping parameters: the nearest-neighbor hopping, denoted by  $t$ , which occurs along the arms of the diamond and dodecagon plaquettes (shown by solid black lines in Fig. 1), and the next-nearest-neighbor hopping, denoted by  $\lambda$ , which connects the two opposite sites across each diamond plaquette (shown by dotted lines in Fig. 1). The electronic properties of the diamond-dodecagon lattice are described by a tight-binding Hamiltonian written in the Wannier basis as,

$$\hat{\mathbf{H}} = \sum_{m,n} \left[ \underbrace{\sum_i \varepsilon_i c_{m,n,i}^\dagger c_{m,n,i}}_{\text{Onsite potential}} + \underbrace{\sum_{\langle i,j \rangle} \left( \mathcal{T}_{ij} c_{m,n,i}^\dagger c_{m,n,j} + \text{h.c.} \right)}_{\text{Intra-cell hopping}} + \underbrace{\sum_{\langle i,j \rangle} \left( \Lambda_{ij} [c_{m,n,i}^\dagger c_{m+1,n,j} + c_{m,n,i}^\dagger c_{m,n+1,j}] + \text{h.c.} \right)}_{\text{Inter-cell hopping}} \right], \quad (1)$$

where  $(m, n)$  denotes the unit cell indices, and  $(i, j) \in \{A, B, C, D, E, F\}$  represent the atomic site indices within each unit cell. The operators  $c_{m,n,i}^\dagger$  and  $c_{m,n,i}$  are the creation and annihilation operators, respectively, for a spinless and non-interacting electron at site  $i$  in the  $(m, n)$ -th unit cell.  $\langle i, j \rangle$  indicates the nearest-neighbor pairs.  $\varepsilon_i$  is the onsite potential of an electron at the  $i$ -th atomic site, and for our model, we set the onsite potentials to be identical across all sites:  $\varepsilon_i = 0$  for all  $i \in \{A, B, C, D, E, F\}$ . We remark that, later in Sec. III, we also explore the effect of an random onsite potential disorder on the FBs in this model.

As prescribed in Eq. (1), we have two different types of hopping parameters for our lattice model, namely, the intra-cell hopping (within a unit cell) and the inter-cell hopping (one unit cell to another unit cell). The intra-cell hopping amplitude takes the values:

$$\mathcal{T}_{ij} = \begin{cases} te^{\pm i\theta} & \text{for the diamond edges (+ for clockwise and - for counterclockwise hopping),} \\ \lambda & \text{for diagonal hopping within a diamond (when } i \text{ and } j \text{ are next-nearest neighbors),} \\ t & \text{for hopping along the dodecagon edges.} \end{cases}$$

where  $\theta$  is the Aharonov-Bohm phase factor given by,  $\theta = 2\pi\Phi/4\Phi_0$ ;  $\Phi_0 = h/e$  being the fundamental flux quantum. The inter-cell hopping amplitude takes the values:

$$\Lambda_{ij} = \begin{cases} t & \text{for nearest-neighbor connections between the adjacent unit cells,} \\ 0 & \text{otherwise.} \end{cases}$$

Throughout our calculation, we set  $t = 1$ , and the energy of the electrons  $E$  is measured in units of  $t$ .

## B. Bloch Hamiltonian

To analyze the band structure of this lattice model, we transform the real-space Hamiltonian in Eq. (1) to momentum space using the discrete Fourier transform:

$$c_{m,n,j} = \frac{1}{\sqrt{N}} \sum_{\mathbf{k}} c_{\mathbf{k},j} e^{i\mathbf{k} \cdot \mathbf{R}_{m,n}}, \quad (2)$$

where  $\mathbf{R}_{m,n}$  is the position vector of the  $(m, n)$ -th unit cell,  $N$  is the total number of unit cells, and the sum runs over all allowed  $\mathbf{k}$  points in the first Brillouin zone. The resulting momentum-space Hamiltonian takes the form:

$$\hat{\mathbf{H}} = \sum_{\mathbf{k}} \Psi_{\mathbf{k}}^\dagger \mathcal{H}(\mathbf{k}) \Psi_{\mathbf{k}}, \quad (3)$$

where the Bloch spinor is defined as:

$$\Psi_{\mathbf{k}}^\dagger = (c_{\mathbf{k},A}^\dagger \ c_{\mathbf{k},B}^\dagger \ c_{\mathbf{k},C}^\dagger \ c_{\mathbf{k},D}^\dagger \ c_{\mathbf{k},E}^\dagger \ c_{\mathbf{k},F}^\dagger). \quad (4)$$

The  $6 \times 6$  Bloch Hamiltonian matrix  $\mathcal{H}(\mathbf{k})$  is given by:

$$\mathcal{H}(\mathbf{k}) = \begin{pmatrix} 0 & te^{i\theta} & \lambda & te^{-i\theta} & t & 0 \\ te^{-i\theta} & 0 & te^{i\theta} & \lambda & 0 & t \\ \lambda & te^{-i\theta} & 0 & te^{i\theta} & te^{ik_x} & 0 \\ te^{i\theta} & \lambda & te^{-i\theta} & 0 & 0 & te^{-ik_y} \\ t & 0 & te^{-ik_x} & 0 & 0 & 0 \\ 0 & t & 0 & te^{ik_y} & 0 & 0 \end{pmatrix}. \quad (5)$$

## C. Band Structure Analysis

Using the Bloch Hamiltonian in Eq. (5), we analyze the evolution of the electronic band structure of the diamond-

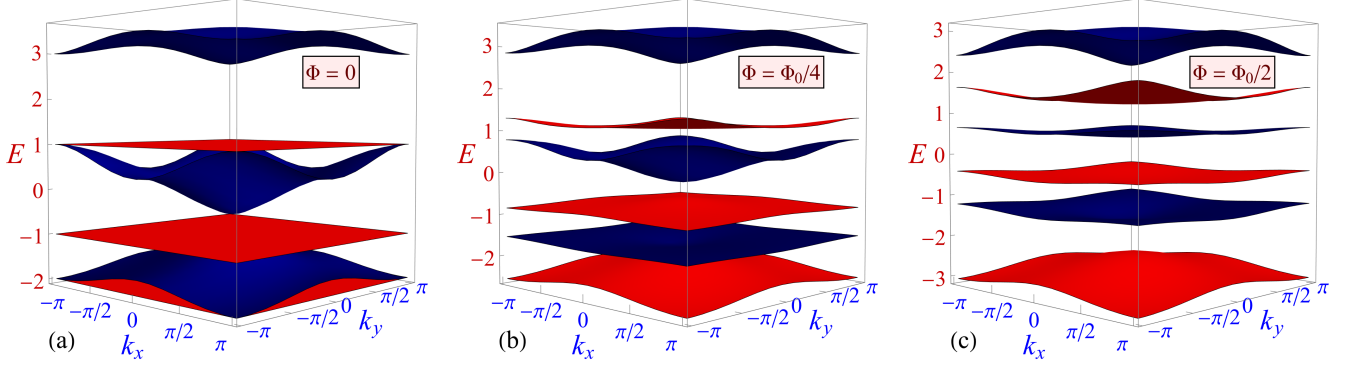


FIG. 2. Electronic band structure for a 2D diamond-dodecagon lattice for three different values of the magnetic flux, *viz.*, (a)  $\Phi = 0$ , (b)  $\Phi = \Phi_0/4$ , and (c)  $\Phi = \Phi_0/2$ . For  $\Phi = 0$ , we have three completely flat, non-dispersive bands appearing in the system marked by the red color, while the remaining three dispersive bands are shown in blue color. For  $\Phi \neq 0$ , gap opens up between all the bands in the system, and the FBs are no longer completely flat; they acquire quasi-flatness. We have set  $\varepsilon_i = 0$  for all sites and  $t = \lambda = 1$ .

dodecagon lattice both in the absence and in the presence of magnetic flux  $\Phi$ . Fig. 2 presents the band dispersion  $E(k_x, k_y)$  for three representative values of the flux:  $\Phi = 0$ ,  $\Phi = \Phi_0/4$ , and  $\Phi = \Phi_0/2$ , highlighting the role of quantum interference, localization, and flux-induced symmetry breaking in the system. The energy eigenvalues of the system are obtained by solving the eigenvalue equation:

$$\det [\mathcal{H}(\mathbf{k}) - E_n(\mathbf{k})\mathbb{I}] = 0. \quad (6)$$

This yields six energy bands  $E_n(\mathbf{k})$  with  $n = 1, 2, \dots, 6$  as functions of the crystal momentum  $\mathbf{k} \equiv (k_x, k_y)$  within the first Brillouin zone.

We first discuss the case of  $\Phi = 0$ . In the absence of magnetic flux  $\Phi$ , the system preserves time-reversal symmetry. The resulting band structure exhibits three perfectly flat bands at the energies  $E_{FB} = -2, -1$ , and  $+1$  (see Fig. 2(a)), characterized by zero group velocity ( $\nabla_{\mathbf{k}} E_n = 0$ ) across the first Brillouin zone. The other three bands are dispersive, spanning the ranges  $E \in [-2, -1]$ ,  $[-1, 1]$ , and  $[2, 3]$ , respectively. These FBs arise from the destructive interference in the hopping pathways, leading to compact localized states (CLS), whose wavefunctions are confined to finite regions. The eigenstates of the dispersive bands are extended and contribute to the bulk transport properties, in contrast to the CLS-based flat bands.

Upon introducing a magnetic flux  $\Phi \neq 0$ , the hopping amplitude  $t$  acquires a complex Peierls phase  $t \rightarrow t e^{\pm i\theta}$ , breaking the time-reversal symmetry and altering the interference conditions. As a result, all the bands are now gapped out from each other, and the perfect flatness of the three FBs does not hold anymore, as they become quasi-flat. This partial delocalization indicates the onset of flux-induced kinetic mixing. The above observations are true for any nonzero values of the flux; for example, here we have shown two such cases – one is for  $\Phi = \Phi_0/4$  and the other one is for  $\Phi = \Phi_0/2$  (see Fig. 2(b) and (c)). Furthermore, under this condition, topological properties

of the system begin to emerge: some of the bands now acquire finite integer values of the Chern numbers, reflecting the broken time-reversal symmetry and a redistribution of the Berry curvature across the Brillouin zone, which is discussed in detail in Sec. IV. This regime marks the transition from the geometrically protected completely FBs to the topologically nontrivial nearly FBs.

The flux-tunable band structure of the diamond-dodecagon lattice demonstrates how magnetic flux can be used to engineer flatness, break the time-reversal symmetry, and induce the topological phases. Such tunable features open the pathways towards realizing the fractional Chern insulators and interaction-driven quantum phases in a diamond-dodecagon lattice model in experimentally accessible platforms, such as photonic lattices and cold atom systems. Before ending this section, we would like to highlight an interesting feature observed in the band structure of this lattice model as a function of the magnetic flux  $\Phi$ . We have found that, one can make any of the six bands of the system completely flat at will for certain specific values of the magnetic flux  $\Phi$ . This is discussed in the Appendix A.

### III. FLAT BANDS AND COMPACT LOCALIZATION

In a translationally invariant system, one typically expects to have the Bloch states with extended wavefunctions. However, under specific conditions dictated by the lattice geometry and the hopping parameters, destructive quantum interference can trap the particles at certain specific values of the energy within a finite region of the corresponding lattice. These trapped states, known as the *compact localized states* (CLS), have wavefunctions that vanish identically outside a finite support region. The existence of CLS is a hallmark of a flat-band system. In this section, we will analyze the structure and formation mechanism of the CLS in the diamond-

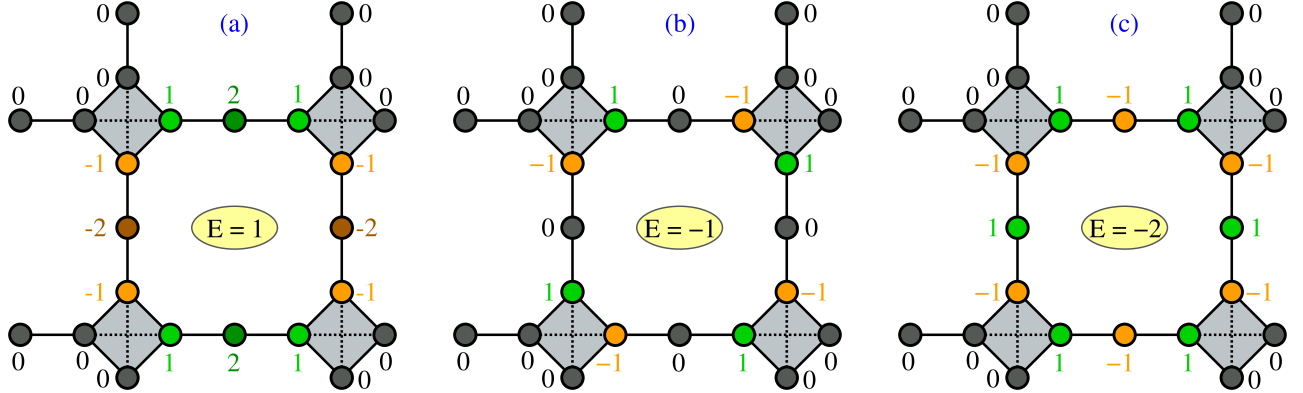


FIG. 3. Distribution of the compact localized states (CLS) corresponding to the flat bands at the energies (a)  $E = 1$ , (b)  $E = -1$ , and (c)  $E = -2$  in the absence of magnetic flux. The black sites denote the nodes with zero wavefunction amplitudes, while the dark and light green sites indicate nonzero positive wavefunction amplitudes (normalized to  $\pm 2$  and  $\pm 1$ , respectively), and the dark and light orange sites indicate nonzero negative wavefunction amplitudes (normalized to  $\pm 2$  and  $\pm 1$ , respectively).

dodecagon lattice model, corresponding to the three exactly FBs observed in the zero-flux band structure (see Fig. 2(a)). These states originate from the geometry-induced destructive quantum interference in the particle hopping pathways and offer deep insight into the microscopic mechanism of FB formation from the real-space point of view.

Fig. 3 presents the real-space wavefunction amplitude distributions of the three CLS corresponding to the FB energies  $E_{FB} = +1, -1$ , and  $-2$  respectively. Each CLS is strictly confined to a small cluster of sites forming a closed loop, which confirms the localized and interference-driven origin of these states. These clusters consist of sites with nonzero wavefunction amplitudes, normalized to  $\pm 2$  and  $\pm 1$ , respectively (shown in dark and light green and orange colors, respectively in Fig. 3(a)-(c)), and they are decoupled from another such cluster with nodes having zero wavefunction amplitudes (shown in black color in Fig. 3(a)-(c)). We point out that, the CLS corresponding to  $E = -1$  is restricted to only one unit cell, whereas the CLS corresponding to  $E = +1$  and  $E = -2$  are spread over four unit cells. Such variation in their amplitude distributions underscores that different FBs may arise from distinct interference patterns and local symmetries.

The CLS amplitude distributions have been obtained using the following difference equation satisfied consistently for all the atomic sites:

$$(E - \varepsilon_i) \psi_i = \sum_j (\mathcal{T}_{ij} + \Lambda_{ij}) \psi_j, \quad (7)$$

with the additional constraint that  $|\psi_{\text{CLS}}(\mathbf{r})|^2 = 0$  outside a finite compact region. Each CLS can be seen as a local eigenmode supported on a small cluster of lattice sites, with vanishing overlap to the neighboring clusters. This ensures that these states remain eigenstates for all the crystal momenta  $\mathbf{k}$ , leading to dispersionless, flat energy bands.

The formation of CLS has profound physical implications. In momentum space, these localized states con-

tribute equally to all  $\mathbf{k}$ -points, resulting in the characteristic flat dispersion. This can be understood from their Fourier transformation relationship: a state perfectly localized in the real space must have a uniform distribution in the momentum space. The FB states are thus fundamentally different from the dispersive band states. While typical Bloch states carry current and contribute to the transport, CLS are immobile by construction. Particles in these states are effectively “caged” by destructive interference, leading to an infinite effective mass and zero group velocity. Unlike Anderson localization, which requires disorder, or Wannier-Stark localization, which needs an external electric field, the CLS in our system emerge due to the intrinsic structure of the lattice. This makes them robust against small perturbations that preserve the underlying symmetries. Similar compact localized modes have been extensively studied in other FB lattice models, such as the Lieb, Kagome, and diamond-octagon lattices. In particular, the role of the interference-induced localization is well-established in these systems, making the diamond-dodecagon lattice a compelling addition to the family of CLS-hosting geometries.

To further characterize the spectral features of the diamond-dodecagon lattice and validate the existence of flat bands, we compute the average density of states (ADOS) using the retarded Green’s function formalism. The ADOS is a crucial quantity that reveals how the energy levels are distributed across the spectrum, offering insight into the presence of the dispersionless states and their robustness against disorder. The ADOS  $\rho(E)$  is calculated numerically using the standard expression:

$$\rho(E) = -\frac{1}{N\pi} \Im [\text{Tr } \mathbf{G}(E)], \quad (8)$$

where  $\mathbf{G}(E)$  is the Green’s function matrix defined by,

$$\mathbf{G}(E) = [(E + i\eta) \mathbf{I} - \mathbf{H}]^{-1}. \quad (9)$$

Here,  $N$  denotes the total number of lattice sites,  $\mathbf{I}$  is

the  $\mathcal{N} \times \mathcal{N}$  identity matrix,  $\mathbf{H}$  is the full tight-binding Hamiltonian matrix in real space, and  $\eta$  is a small broadening parameter (taken to be  $\sim 10^{-3}$  in our numerical simulations) ensuring convergence and mimicking finite-lifetime effects. The imaginary part of the trace of  $\mathbf{G}(E)$  captures the total spectral weight at the energy  $E$ .

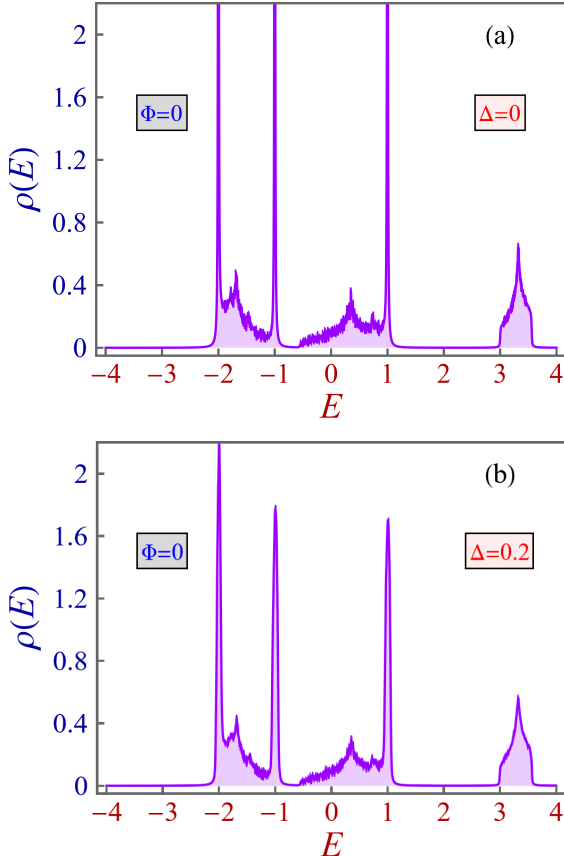


FIG. 4. The variation of the average density of states (ADOS)  $\rho(E)$  of the system as a function of the energy ( $E$ ) for  $\Phi = 0$ . (a) is for the perfectly ordered system and (b) is for a random disordered distribution of the onsite energies with a disorder strength  $\Delta = 0.2$  (measured in units of  $t$ ). The sharp peaks in the spectrum indicate the flat band states. The system size considered here is  $30 \times 30$  unit cells (*i.e.*,  $\mathcal{N} = 5400$  sites).

Fig. 4 displays the ADOS computed for the two scenarios: (a) corresponds to the perfectly ordered lattice ( $\Delta = 0$ ) and (b) shows the disordered case with onsite disorder strength  $\Delta = 0.2$ , where the onsite energies are chosen randomly from a uniform distribution in the interval  $[-\Delta/2, \Delta/2]$ .

(a) *Ordered System ( $\Delta = 0$ )*: In the absence of any disorder in the system, the ADOS reveals three sharp delta-function-like peaks at  $E = -2$ ,  $E = -1$ , and  $E = +1$  (see Fig. 4(a)). These peaks are the direct signatures of the three perfectly flat bands present in the band structure (cf. Fig. 2(a)). The delta-function-like nature of these peaks arises due to the macroscopic degeneracy and zero bandwidth of the FBs, resulting in a diverging density of states. Each flat band contributes to a singularity in

$\rho(E)$ , indicating that a macroscopic number of states are concentrated at a single energy level. The appearance of these sharp peaks in the ADOS spectrum corresponding to the FB energies corroborates the CLS constructions, in which the nonzero wavefunction amplitudes are localized over small clusters of lattice sites in the real-space. Apart from the sharp FB peaks, the ADOS also shows broader continuum structures, which correspond to the dispersive bands. These regions reflect the energy intervals over which the extended Bloch states are spread.

(b) *Disordered System ( $\Delta = 0.2$ )*: Introducing a finite random onsite disorder in the system breaks the perfect translational invariance and perturbs the FB states. Here, we have chosen a random onsite disorder of strength  $\Delta = 0.2$  (measured in units of  $t$ ). As a result, the delta-function-like peaks in the ADOS spectrum start to broaden into finite-width peaks (see Fig. 4(b)). However, the spectral remnants of the FBs are still visible. Physically, disorder introduces hybridization between the CLS and the extended states, lifting the perfect degeneracy and leading to a finite dispersion. This is reflected in the smearing of the ADOS peaks. Despite the smearing, the remnants of high spectral weight around the FB energies still persist, implying that the CLS-based FB physics remains relevant even in the weakly disordered regime. This robustness is essential, as in real systems, the presence of disorder is inevitable. The high density of states at the FB energies also enhances interaction effects, even at moderate coupling strengths, making the system a promising candidate for realizing correlated states, such as ferromagnetism or fractional Chern insulators in the presence of interactions and topology.

#### IV. CHARACTERIZATION OF THE TOPOLOGICAL STATES

In this section, we will present the nontrivial topological properties of the diamond-dodecagon lattice model. Topological properties in a lattice model refers to the certain global, symmetry-protected features of its band structure, which are in general robust against the local perturbations, like small disorder, weak interaction etc. Topological properties of a lattice model can be perceived by studying its Bloch Hamiltonian  $\mathcal{H}(\mathbf{k})$ , as the topological properties emerge in the system when the Bloch eigenstates of the Hamiltonian  $\mathcal{H}(\mathbf{k})$  cannot be smoothly defined over the entire Brillouin zone of the lattice. This can be quantified by calculating certain *topological invariant* quantities like the Berry curvatures and Chern numbers corresponding to all the energy bands in the system [55, 56]. It is to be noted that, topology is a property of the eigenstates of the Hamiltonian of the system and not of its eigenvalues.

The Berry curvature corresponding to each the band of the present lattice model can be computed using the

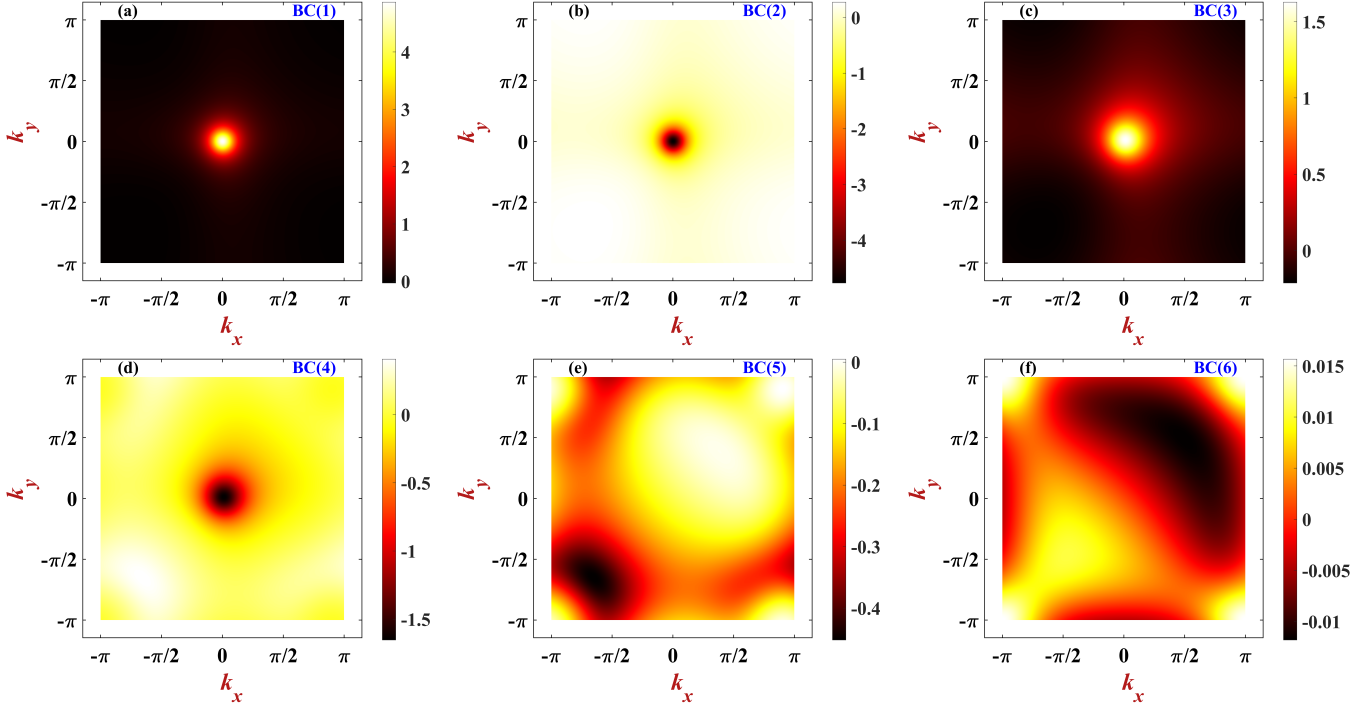


FIG. 5. Distribution of the Berry curvatures (BC) in the first Brillouin zone for all the six bands ( $n = 1$  to  $6$ ) in the diamond-dodecagon lattice at a magnetic flux  $\Phi = \Phi_0/4$ , corresponding to the band structure shown in Fig. 2(b). The upper panel corresponds to the band index  $n = 1$  to  $3$  and the lower panel corresponds to the band index  $n = 4$  to  $6$ . The system exhibits nontrivial topology with Chern numbers  $C_1 = +1$  and  $C_5 = -1$ , while the remaining bands are topologically trivial ( $C_n = 0$  for  $n = 2, 3, 4, 6$ ).

following expressions:

$$\Omega_n(\mathbf{k}) = \sum_{E_m(\neq E_n)} \frac{-2 \Im(\mathcal{F}_{nm}^x \mathcal{F}_{mn}^y)}{[E_n(\mathbf{k}) - E_m(\mathbf{k})]^2}, \quad (10)$$

$$\text{where } \mathcal{F}_{nm}^x = \langle \psi_n(\mathbf{k}) | \frac{\partial \mathcal{H}(\mathbf{k})}{\partial k_x} | \psi_m(\mathbf{k}) \rangle$$

$$\text{and } \mathcal{F}_{mn}^y = \langle \psi_m(\mathbf{k}) | \frac{\partial \mathcal{H}(\mathbf{k})}{\partial k_y} | \psi_n(\mathbf{k}) \rangle.$$

Here,  $|\psi_n(\mathbf{k})\rangle$  is the eigenstate of the Bloch Hamiltonian  $\mathcal{H}(\mathbf{k})$  in Eq. (5) with an eigenvalue  $E_n(\mathbf{k})$ , for the  $n$ -th band of the system. We can easily obtain the Chern number of the  $n$ -th band of the system by taking the summation over all the values of  $\Omega_n(\mathbf{k})$  over the first Brillouin zone ( $BZ$ ) of the lattice model, and is given by,

$$C_n = \frac{1}{2\pi} \int_{BZ} \Omega_n(\mathbf{k}) d\mathbf{k}. \quad (11)$$

It is apparent from the Eq. (10) that, the Berry curvature diverges if there is any band-touching between the energy bands of the system. Therefore, in order to evaluate the Berry curvatures and the Chern numbers for all the bands of the system, we need to open up the band-gap between all the energy bands in the system. For our model, we do so by tuning the nonzero values of the external magnetic

flux  $\Phi$  through the diamond plaquettes, which breaks the time-reversal symmetry of system and generates band-gaps between all the bands (cf. Fig. 2(b) and (c)).

Under this condition, we have computed the Berry curvatures and hence the Chern numbers for all the isolated bands of the system to understand the topological character of the Bloch eigenstates in this lattice model. We have chosen two different nonzero values of the magnetic flux:  $\Phi = \Phi_0/4$  and  $\Phi = \Phi_0/2$  to obtain the numerical results for the topological invariants of the system. For the case of  $\Phi = \Phi_0/4$ , the numerical plots of the Berry curvature distributions in the  $\mathbf{k}$ -space (first Brillouin zone) corresponding to all the six bands ( $n = 1$  to  $6$ ) are displayed in Fig. 5(a)-(f). The corresponding values of the Chern numbers are  $C_n = \{+1, 0, 0, 0, -1, 0\}$ . Thus, it is clearly evident that, the lowest band ( $n = 1$ ) and the fifth band ( $n = 5$ ) exhibit nontrivial topological character with nonzero integer values of the Chern numbers equal to  $C_1 = +1$  and  $C_5 = -1$ , respectively. We have also computed the Berry curvature distributions for all the bands in the system for the flux  $\Phi = \Phi_0/2$ , which are shown in Fig. 6(a)-(f). In this case, the corresponding values of the Chern numbers for the different bands are  $C_n = \{0, +1, 0, 0, -1, 0\}$ . Interestingly, now we observe that, the second band ( $n = 2$ ) and the fifth band ( $n = 5$ ) show nonzero integer values of the Chern numbers,  $C_2 = +1$  and  $C_5 = -1$ , respectively, exhibiting their topological character. We remark that, it indi-

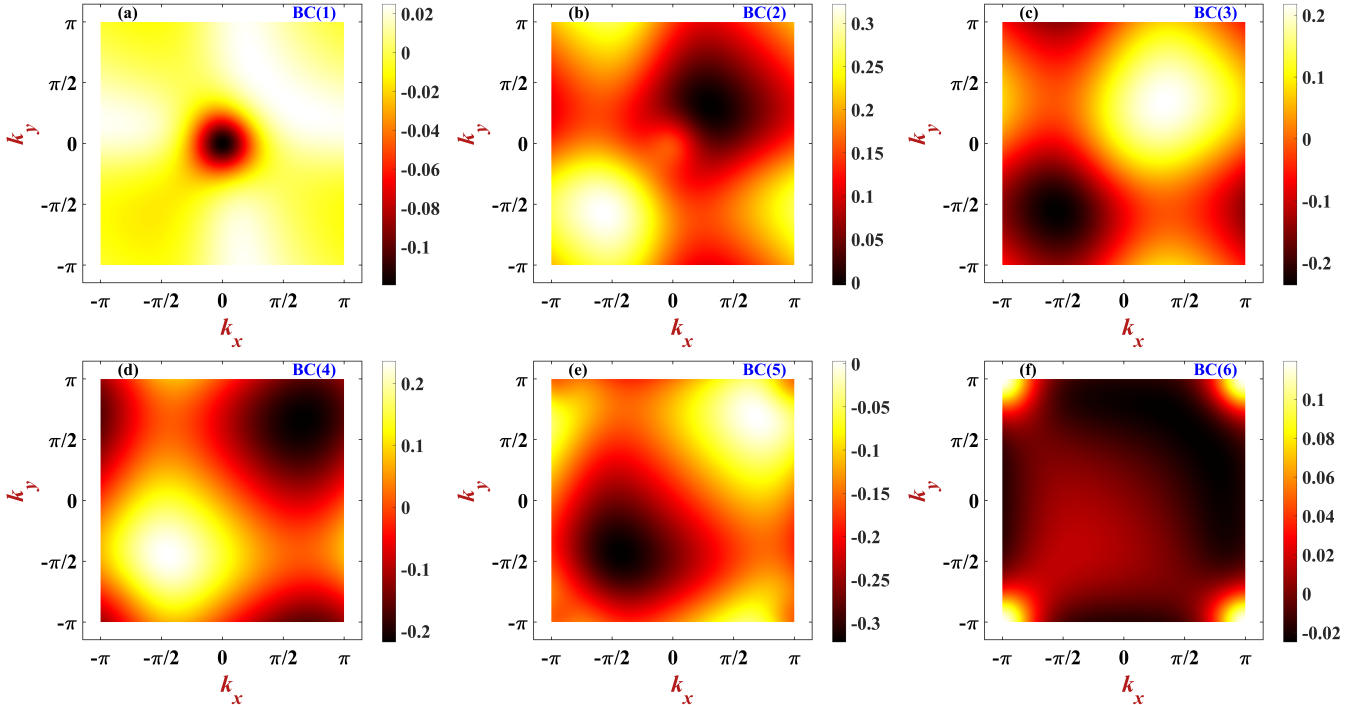


FIG. 6. Distribution of the Berry curvatures (BC) in the first Brillouin zone for all the six bands ( $n = 1$  to  $6$ ) in the diamond-dodecagon lattice at a magnetic flux  $\Phi = \Phi_0/2$ , corresponding to the band structure shown in Fig. 2(c). The upper panel represents the plots for the band index  $n = 1$  to  $3$  and the lower panel shows the plots for the band index  $n = 4$  to  $6$ . The second and the fifth bands exhibits nontrivial topological character with integer values of the Chern numbers  $C_2 = +1$  and  $C_5 = -1$ , respectively, while the remaining bands are of topologically trivial in nature ( $C_n = 0$  for  $n = 1, 3, 4, 6$ ).

cates towards a topological phase transition for this lattice model. We have also computed the Berry curvature distributions and the corresponding values of the Chern numbers for this lattice model with various other nonzero values of the flux, and in all those cases, the system exhibits nontrivial topological behavior. However, to save space, we refrain ourselves from showing those results.

Before we end this section, we would like to emphasize on the fact that, such 2D lattice models exhibiting nearly flat topological bands with nonzero integer values of the Chern numbers are very useful for the realization of the quantum Hall states in lattice settings, which has been exhibited earlier in other interesting 2D lattice models also [21, 22, 50–52, 56].

## V. TRANSPORT PROPERTIES IN A FINITE-SIZE SYSTEM

In this section, we explore the transport properties of a finite-size diamond-dodecagon lattice setup as a function of the externally tunable magnetic flux  $\Phi$  and the energy ( $E$ ) of the incoming electrons. For this computation, we consider a finite segment of the 2D diamond-dodecagon lattice, composed of  $10 \times 10$  arrays of unit cells (having 600 atomic sites), attached in-between two 2D semi-infinite leads along the  $\pm x$  directions (see Fig. 7(a)). The central scattering region (black sites and bonds) is

bounded by two identical leads (red sites and bonds), modelled as the perfect repetitions of the unit cell geometry, enabling coherent quantum transport along the longitudinal direction.

The transport characteristics are calculated using the *scattering matrix formalism* [57, 58], as implemented in the *Kwant* package [59], which enables the efficient computation of the transmission probabilities for any arbitrary tight-binding lattice geometries connected to external leads [60–63]. Mathematically, the scattering matrix  $S$  relates the incoming and the outgoing modes in the leads, and can be used to extract the total transmission probability between any two terminals. This method is formally equivalent to the non-equilibrium Green's function (NEGF) technique, as established by the Fisher-Lee relation [64], where the self-energy terms from the semi-infinite leads account for their influence on the central region as plane-wave superpositions.

The total transmission probability from lead  $p$  (known as the *source*) to lead  $q$  (known as the *drain*) at an energy  $E$  is computed as [59]:

$$T(E) = \sum_{a \in p} \sum_{b \in q} |S_{pq}^{(ba)}(E)|^2, \quad (12)$$

where  $S_{pq}^{(ba)}$  is the scattering matrix element describing the amplitude of a wave transmitted from mode  $a$  in the lead  $p$  to mode  $b$  in the lead  $q$ . To obtain the scattering

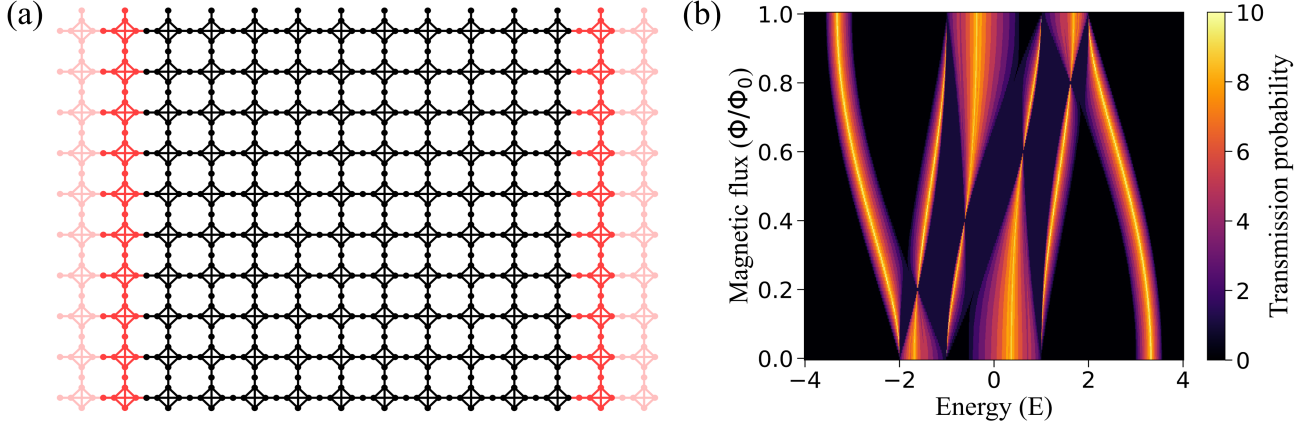


FIG. 7. (a) Schematic diagram of a finite-size  $10 \times 10$  diamond-dodecagon lattice scattering setup. The black dots and connecting lines denote the central scattering region, while the red sites and links indicate the semi-infinite leads attached along the  $\pm x$  directions. (b) Density-plot of the two-terminal transmission probability  $T(E, \Phi)$  through the finite-size  $10 \times 10$  diamond-dodecagon lattice system as a function of magnetic flux  $\Phi$  measured in units of  $\Phi_0$  (vertical axis) and the energy of the incoming electrons  $E$  (horizontal axis). The color scale (shown at the right) encodes  $T$  from 0 (dark) to its maximum (bright). The computation is done at zero temperature and we set  $t = \lambda = 1.0$  eV.

matrix  $S$ , the time-independent Schrödinger equation

$$\mathbf{H}_{\text{full}}\psi_i = E\psi_i \quad (13)$$

is solved, where  $\mathbf{H}_{\text{full}}$  is the full Hamiltonian of the system written in a block-tridiagonal form that includes the Hamiltonian of the scattering region, the lead unit cells, and the coupling matrices. The wave function  $\psi_i$  describes the state of the system inside the scattering region, matched to the propagating and evanescent modes in the leads.

Using the scattering matrix approach outlined in Eq. (12), we have computed the transmission characteristics for the system depicted in Fig. 7(a) as a function of the magnetic flux  $\Phi$  and the energy ( $E$ ) of the electron as shown in Fig. 7(b). It shows an interesting and rich phase diagram, exhibiting regions of complete transmission suppression (dark spots in Fig. 7(b)) coexisting with regions of ballistic transmission (bright spots in Fig. 7(b)), and also re-entrant transitions in between them as a function of the magnetic flux  $\Phi$  and the energy ( $E$ ) of the electron. It unfolds an interesting possibility of opening and closing the conducting channels in this system by tuning the externally controllable parameter  $\Phi$ . In addition to this, the complete suppression of the transmission probabilities corresponding to the FB energies is also indicative of the fact that they form the CLS and hence do not contribute to the transport.

This analysis highlights the diamond-dodecagon lattice as a tunable quantum platform, where both FB-induced localization and topological effects can be investigated via the transport signatures of the system. The ability to modulate the transmission spectrum with an external magnetic flux suggests potential applications of this lattice model in programmable quantum devices, synthetic gauge field simulations, and topological insulator analogs in photonic or ultracold atom settings.

## VI. SUMMARY AND FUTURE OUTLOOK

In this work, we have presented a comprehensive theoretical study of a novel 2D tight-binding diamond-dodecagon lattice model, exploring its various intriguing features in the context of flat-band physics, topological properties and transport characteristics. We have shown that an interplay between the lattice geometry, externally tunable magnetic flux, and the quantum interference effect brings out these interesting properties in this lattice model. It has been shown that this lattice model exhibits multiple completely flat bands in its band structure, supported by exact constructions of the corresponding compact localized states in the real space. The computation of the density of states accomplishes that, these flat bands are very robust in their character in the presence of a weak disorder in the system.

Under the application of an external magnetic flux, the band gap opens up between all the bands in the system, making these completely flat bands into quasi-flat bands with nontrivial topological features. These nontrivial topological features are marked by the computation of the Berry curvatures and the Chern numbers for those topologically nontrivial bands. This opens up an interesting platform for exploring the quantum Hall physics and Chern insulator in this lattice model, both without and with interaction. The transmission characteristics evaluated for this system using the scattering matrix formalism also exhibit a rich pattern with multiple re-entrant transitions between the completely ballistic and the zero transmission domains as a function of the externally controllable magnetic flux. This indicates an interesting possibility of utilizing this system for potential applications in quantum sensor devices. Additionally, flux tunability of the spectrum offers dynamic con-

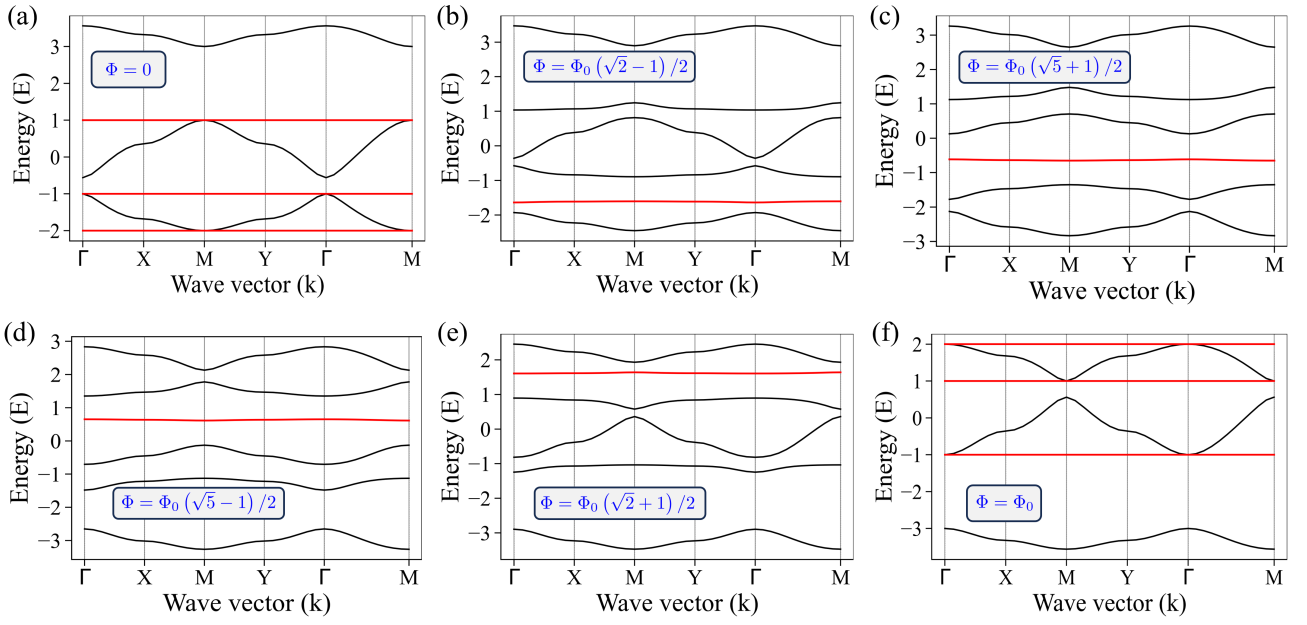


FIG. A.1. Variation of the electronic band structure in the diamond-dodecagon lattice as a function of magnetic flux  $\Phi$ . The six figures show the energy dispersion along high-symmetry directions in the Brillouin zone for six different flux values: (a)  $\Phi = 0$ , (b)  $\Phi = \Phi_0(\sqrt{2} - 1)/2$ , (c)  $\Phi = \Phi_0(\sqrt{5} + 1)/2$ , (d)  $\Phi = \Phi_0(\sqrt{5} - 1)/2$ , (e)  $\Phi = \Phi_0(\sqrt{2} + 1)/2$ , and (f)  $\Phi = \Phi_0$ , where  $\Phi_0$  is the fundamental flux quantum. The red horizontal lines indicate the perfectly flat bands with zero group velocity, while the black curves represent the dispersive bands. It is clearly visible from these plots that we can make any of the six bands completely flat at will by tuning certain specific values of the flux  $\Phi$ .

trol over transport, essential for exploring flux-induced topological transitions and magnetotransport responses.

The proposed diamond-dodecagon lattice model offers fertile ground for various intriguing future research directions. The ability to systematically control both the flatness and topological properties of multiple bands makes the diamond-dodecagon lattice particularly attractive for exploring various strongly correlated topological phenomena. Additionally, incorporating spin-orbit coupling in this model could reveal richer topological phases, including the time-reversal invariant topological insulators. Furthermore, periodic driving (Floquet engineering) may dynamically modulate the band topology, opening avenues to explore the non-equilibrium topological states. From the experimental perspective, the diamond-dodecagon lattice can be realized in real-life experiments in the field of photonics using the laser-induced single-mode photonic waveguide arrays to explore the corresponding topological photonics phenomena.

## ACKNOWLEDGMENTS

BP would like to acknowledge the funding from the Nagaland University through a minor start-up research grant.

## Appendix A: Magnetic flux-driven evolution of FBs

In this appendix, we present a systematic evolution of the electronic band structure in the diamond-dodecagon lattice as a function of the magnetic flux  $\Phi$ . We would like to point out a very interesting aspect observed in the band structure of this lattice model: One can systematically make any of the six bands in the band structure of this lattice model perfectly flat at will by tuning the value of the external magnetic flux  $\Phi$ . This interesting feature is highlighted in Fig. A.1. We remark that the energy dispersions in Fig. A.1 are plotted along the high-symmetry directions in the Brillouin zone.

As discussed previously, at  $\Phi = 0$ , we find that the lowest band of the system exhibits perfect flatness along with two other complete flat bands also (see Fig. A.1(a)). As we tune the value of  $\Phi = \Phi_0(\sqrt{2} - 1)/2$ , we observe that the second band of the system becomes completely flat, while for  $\Phi = \Phi_0(\sqrt{5} + 1)/2$ , the third band of the system turns into a complete flat band (see Fig. A.1(b) and (c)). Similarly, for  $\Phi = \Phi_0(\sqrt{5} - 1)/2$  and  $\Phi = \Phi_0(\sqrt{2} + 1)/2$ , the fourth and the fifth bands of the system, respectively, exhibit perfect flatness (see Fig. A.1(d) and (e)). Finally for  $\Phi = \Phi_0$ , the topmost band of the system transforms into a completely flat band along with two other perfectly flat bands in the spectrum (see Fig. A.1(f)). This interesting feature of controlling the position of the completely flat band in the band structure of the system at will offers us a very unique situation, where one can set the Fermi

energy of the system to be aligned with flat band energy

and study various strongly correlated phenomena for this lattice model at different filling factors.

---

[1] D. Leykam, A. Andreanov, and S. Flach, *Adv. Phys. X* **3**, 1473052 (2018).

[2] L. Tang, D. Song, S. Xia, S. Xia, J. Ma, W. Yan, Y. Hu, J. Xu, D. Leykam, and Z. Chen, *Nanophotonics* **9**, 1161 (2020).

[3] R. A. Vicencio Poblete, *Adv. Phys. X* **6**, 1878057 (2021).

[4] N. B. Kopnin, T. T. Heikkilä, and G. E. Volovik, *Phys. Rev. B* **83**, 220503(R) (2011).

[5] V. J. Kauppila, F. Aikebaier, and T. T. Heikkilä, *Phys. Rev. B* **93**, 214505 (2016).

[6] M. Thumin and G. Bouzerar, *Phys. Rev. B* **107**, 214508 (2023).

[7] G. Bouzerar and M. Thumin, *Phys. Rev. B* **111**, L020506 (2025).

[8] M. Thumin and G. Bouzerar, *SciPost Phys.* **18**, 025 (2025).

[9] A. Mielke, *J. Phys. A Math. Gen.* **24**, L73 (1991).

[10] H. Tasaki, *Phys. Rev. Lett.* **69**, 1608 (1992).

[11] M. Maksymenko, A. Honecker, R. Moessner, J. Richter, and O. Derzhko, *Phys. Rev. Lett.* **109**, 096404 (2012).

[12] G. Bouzerar, *Phys. Rev. B* **107**, 184441 (2023).

[13] Z. Liu, E. J. Bergholtz, H. Fan, and A. M. Läuchli, *Phys. Rev. Lett.* **109**, 186805 (2012).

[14] E. J. Bergholtz and Z. Liu, *Int. J. Mod. Phys. B* **27**, 1330017 (2013).

[15] A. Abouelkomans, Z. Liu, and E. J. Bergholtz, *Phys. Rev. Lett.* **124**, 106803 (2020).

[16] K. v. Klitzing, G. Dorda, and M. Pepper, *Phys. Rev. Lett.* **45**, 494 (1980).

[17] R. B. Laughlin, *Phys. Rev. B* **23**, 5632(R) (1981).

[18] R. B. Laughlin, *Phys. Rev. Lett.* **50**, 1395 (1983).

[19] A. Ramachandran, A. Andreanov, and S. Flach, *Phys. Rev. B* **96**, 161104(R) (2017).

[20] J.-W. Rhim and B.-J. Yang, *Adv. Phys. X* **6**, 1901606 (2021).

[21] B. Pal, *Phys. Rev. B* **98**, 245116 (2018).

[22] B. Pal and G. Bouzerar, *J. Phys.: Condens. Matter* **37**, 135503 (2025).

[23] B. Sutherland, *Phys. Rev. B* **34**, 5208 (1986).

[24] A. Julku, S. Peotta, T. I. Vanhala, D.-H. Kim2, and P. Törmä, *Phys. Rev. Lett.* **117**, 045303 (2016).

[25] W. Beugeling, J. C. Everts, and C. Morais Smith, *Phys. Rev. B* **86**, 195129 (2012).

[26] D. Green, L. Santos, and C. Chamon, *Phys. Rev. B* **82**, 075104 (2010).

[27] S. Mondal and S. Basu, *Phys. Rev. B* **107**, 035421 (2023).

[28] S. Mukherjee and R. R. Thomson, *Opt. Lett.* **40**, 5443 (2015).

[29] A. M. Marques, D. Viedma, V. Ahufinge, and R. G. Dias, *Commun. Phys.* **7**, 387 (2024).

[30] A. Mukherjee, A. Nandy, S. Sil, and A. Chakrabarti, *J. Phys.: Condens. Matter* **33**, 035502 (2021).

[31] A. Bhattacharya and B. Pal, *Phys. Rev. B* **100**, 235145 (2019).

[32] B. Pal and K. Saha, *Phys. Rev. B* **97**, 195101 (2018).

[33] W. Yan, H. Zhong, D. Song, Y. Zhang, S. Xia, L. Tang, D. Leykam, and Z. Chen, *Adv. Opt. Mater.* **8**, 1902174 (2020).

[34] L. Song, S. Gao, J. Ma, L. Tang, D. Song, Y. Li, and Z. Chen, *Opt. Lett.* **48**, 5947 (2023).

[35] H. Hanafi, P. Menz, A. McWilliam, J. Imbrock, and C. Denz, *APL Photon.* **7**, 111301 (2022).

[36] H. Hanafi, P. Menz, and C. Denz, *Adv. Opt. Mater.* **10**, 2102523 (2022).

[37] Y. Xie, L. Song, W. Yan, S. Xia, L. Tang, D. Song, J.-W. Rhim, and Z. Chen, *APL Photon.* **6**, 116104 (2021).

[38] L. Song, Y. Xie, S. Xia, L. Tang, D. Song, J.-W. Rhim, and Z. Chen, *Laser Photon. Rev.* **17**, 2200315 (2023).

[39] R. A. Vicencio, C. Cantillano, L. Morales-Inostroza, B. Real, C. Mejía-Cortés, S. Weimann, A. Szameit, and M. I. Molina, *Phys. Rev. Lett.* **114**, 245503 (2015).

[40] S. Mukherjee, A. Spracklen, D. Choudhury, N. Goldman, P. Öhberg, E. Andersson, and R. R. Thomson, *Phys. Rev. Lett.* **114**, 245504 (2015).

[41] S. Mukherjee, M. Di Liberto, P. Öhberg, R. R. Thomson, and N. Goldman, *Phys. Rev. Lett.* **121**, 075502 (2018).

[42] G. Cáceres-Aravena, D. Guzmán-Silva, I. Salinas, and R. A. Vicencio, *Phys. Rev. Lett.* **128**, 256602 (2022).

[43] N. Goldman, D. F. Urban, and D. Bercioux, *Phys. Rev. A* **83**, 063601 (2011).

[44] Y. He, R. Mao, H. Cai, J.-X. Zhang, Y. Li, L. Yuan, S.-Y. Zhu, and D.-W. Wang, *Phys. Rev. Lett.* **126**, 103601 (2021).

[45] H. Li, Z. Dong, S. Longhi, Q. Liang, D. Xie, and B. Yan, *Phys. Rev. Lett.* **129**, 220403 (2022).

[46] L. Balents, C. R. Dean, D. K. Efetov, and A. F. Young, *Nat. Phys.* **16**, 725 (2020).

[47] Z. Zhang, Y. Wang, K. Watanabe, T. Taniguchi, K. Ueno, E. Tutuc, and B. J. LeRoy, *Nat. Phys.* **16**, 1093 (2020).

[48] H. Li *et al.*, *Nat. Mater.* **20**, 945 (2021).

[49] C. Danieli, J. Liu, R. A. Römer, and R. A. Vicencio, *Phys. Rev. Lett.* **136**, 066302 (2026).

[50] E. Tang, J.-W. Mei, and X.-G. Wen, *Phys. Rev. Lett.* **106**, 236802 (2011).

[51] K. Sun, Z. Gu, H. Katsura, and S. Das Sarma, *Phys. Rev. Lett.* **106**, 236803 (2011).

[52] T. Neupert, L. Santos, C. Chamon, and C. Mudry, *Phys. Rev. Lett.* **106**, 236804 (2011).

[53] L. Chen, T. Mazaheri, A. Seidel, and X. Tang, *J. Phys. A: Math. Theor.* **47**, 152001 (2014).

[54] Y. Aharonov and D. Bohm, *Phys. Rev.* **115**, 485 (1959).

[55] F. D. M. Haldane, *Phys. Rev. Lett.* **93**, 206602 (2004).

[56] M. Chen and S. Wan, *J. Phys.: Condens. Matter* **24**, 325502 (2012).

[57] S. Datta, *Electronic Transport in Mesoscopic Systems* (Cambridge University Press, Cambridge, 1995).

[58] S. Datta, *Quantum Transport: Atom to Transistor* (Cambridge University Press, Cambridge, 2005).

[59] C. W. Groth, M. Wimmer, A. R. Akhmerov, and X. Waintal, *New J. Phys.* **16**, 063065 (2014).

[60] J. Majhi, S. K. Maiti, and S. Ganguly, *Nanotechnology* **33**, 255704 (2022).

[61] M. Istan, C. Groth, and X. Waintal, *Phys. Rev. Res.* **1**, 033188 (2019).

- [62] X. Waintal, M. Wimmer, A. R. Akhmerov, C. Groth, B. K. Nikolić, M. Istan, T. Ö. Rosdahl, and D. Varjas, “Computational quantum transport”, [arXiv:2407.16257](https://arxiv.org/abs/2407.16257) (2024).
- [63] L. L. Li and F. M. Peeters, *Phys. Rev. B* **97**, 075414 (2018).
- [64] D. S. Fisher and P. A. Lee, *Phys. Rev. B* **23**, 6851 (1981).